



Inertial particle focusing dynamics in a trapezoidal straight microchannel: application to particle filtration

Reza Moloudi^{1,2} · Steve Oh³ · Chun Yang¹ · Majid Ebrahimi Warkiani^{4,5,6} · May Win Naing²

Received: 18 December 2017 / Accepted: 7 February 2018 / Published online: 5 March 2018
© Springer-Verlag GmbH Germany, part of Springer Nature 2018

Abstract

Inertial microfluidics has emerged recently as a promising tool for high-throughput manipulation of particles and cells for a wide range of flow cytometric tasks including cell separation/filtration, cell counting, and mechanical phenotyping. Inertial focusing is profoundly reliant on the cross-sectional shape of channel and its impacts on not only the shear field but also the wall-effect lift force near the wall region. In this study, particle focusing dynamics inside trapezoidal straight microchannels was first studied systematically for a broad range of channel Re number ($20 < \text{Re} < 800$). The altered axial velocity profile and consequently new shear force arrangement led to a cross-lateral movement of equilibration toward the longer side wall when the rectangular straight channel was changed to a trapezoid; however, the lateral focusing started to move backward toward the middle and the shorter side wall, depending on particle clogging ratio, channel aspect ratio, and slope of slanted wall, as the channel Reynolds number further increased ($\text{Re} > 50$). Remarkably, an almost complete transition of major focusing from the longer side wall to the shorter side wall was found for large-sized particles of clogging ratio $K \sim 0.9$ ($K = a/H_{\min}$) when Re increased noticeably to ~ 650 . Finally, based on our findings, a trapezoidal straight channel along with a bifurcation was designed and applied for continuous filtration of a broad range of particle size ($0.3 < K < 1$) exiting through the longer wall outlet with $\sim 99\%$ efficiency ($\text{Re} < 100$).

Keywords Inertial microfluidics · Straight microchannel · Trapezoidal · Filtration · Cell/particle sorting

1 Introduction

Separation of particles based on size is an essential step in numerous industrial and biomedical processes. Filtration, sedimentation, and centrifugation techniques are frequently

used to separate and classify particles and cells. But performance of these approaches is generally poor when the particle size and the size difference between target and non-target particles are small (Bhagat et al. 2010b). Furthermore, clogging and fouling of device components is inevitable, which fundamentally limits the efficiency and reliability of the filtration process (Warkiani et al. 2012). The development of microfluidics in the past 15 years has brought about

Electronic supplementary material The online version of this article (<https://doi.org/10.1007/s10404-018-2045-5>) contains supplementary material, which is available to authorized users.

✉ Majid Ebrahimi Warkiani
Majid.Warkiani@uts.edu.au

✉ May Win Naing
winnaingm@SIMTech.a-star.edu.sg

¹ School of Mechanical and Aerospace Engineering, Nanyang Technological University (NTU), 50 Nanyang Avenue, Singapore 639798, Singapore

² Bio-Manufacturing Programme, Singapore Institute of Manufacturing Technology (SIMTech), Agency for Science, Technology and Research (A*STAR), 2 Fusionopolis Way #08-04, Innovis, Singapore 138634, Singapore

³ Stem Cell Group, Bioprocessing Technology Institute, Centros, Singapore 138668, Singapore

⁴ School of Biomedical Engineering, University of Technology Sydney, Sydney, NSW 2007, Australia

⁵ School of Medical and Health Sciences, Edith Cowan University, Perth, Australia

⁶ Institute of Molecular Medicine, Sechenov First Moscow State University, Moscow 119991, Russia

new methods for the separation and selection of microparticles through precise control of fluid flow. Among all existing microfluidic systems, inertial microfluidics (IMF) has experienced substantial growth in many applications such as cell detection and isolation (Bhagat et al. 2010b; Hur et al. 2011), cytometry (Bhagat et al. 2010c), multiplexed bio-assays (Chen et al. 2008; Situma et al. 2006; Wang and Li 2011), and fluid mixing (Sudarsan and Ugaz 2006). As a passive technique, it manipulates cells and particles (by taking advantages of hydrodynamic forces) in microchannels with variety of cross sections (i.e., square, rectangular, trapezoidal, triangular, and circular), in the absence of an externally applied field, and combines the benefits of a passive approach with extremely high-throughput and yield (Amini et al. 2014; Zhang et al. 2016). There are also a plethora of active techniques such as magnetophoresis (Murthy 1999; Pamme and Manz 2004), dielectrophoresis (Kralj et al. 2006; Voldman 2006; Zhu et al. 2010), and acoustophoresis (Destgeer et al. 2013; Ma et al. 2016; Nilsson et al. 2004; Petersson et al. 2007) for particle separation. There are comprehensive and insightful reviews about these different techniques later in this literature (Di Carlo 2009; Sajeesh and Sen 2014; Warkiani et al. 2015).

There are basically two types of IMF including structured and non-structured channels (Amini et al. 2014). Any pattern, in non-structured channels, such as spiral (Bhagat et al. 2008a; Guan et al. 2013; Martel and Toner 2013), asymmetric (Di Carlo et al. 2007), serpentine (Zhang et al. 2014a, b), and contraction/expansion (Lee et al. 2011; Park et al. 2009; Sim et al. 2011; Wu et al. 2016) induces a secondary flow, which is perpendicular to the main flow direction. The channel length in such device can be increased without significantly increasing the size of the device and compromising its portability due to the radial geometry (Yang et al. 2011). Although structured channels have been widely used in recent years, straight channel has some benefits such as small footprint, ease of parallelization, simplicity in fabrication and design principles (Zhang et al. 2014b).

Inertial migration of neutrally buoyant particles across the streamline flowing through a channel was first observed by Segré and Silberberg (1961)—it was called *tubular pinch effect* (Segré and Silberberg 1961, 1962), formation of focused ring-like particle region that is $\sim 60\%$ away from center of channel. Initially, this phenomenon was conceived as the interaction between two major forces: shear-gradient and wall-induced lift forces which were analytically proved by applying perturbation method (Asmolov 1999; Ho and Leal 1974; Schonberg and Hinch 1989; Vasseur and Cox 1976). However, this model is not able to explain the focusing position in non-circular cross-section microchannels. Cross-lateral migration of particles inside square and rectangular microchannels experimentally proved the wall-effect lift force when the inertial effect (i.e., particle Reynolds

number $R_p = R_e a^2 / D_H^2$ where R_e is channel Reynolds number, a is particle diameter, and D_H is the hydraulic diameter of channel) goes beyond a certain threshold, $R_p \sim 1$ (Bhagat et al. 2008c; Di Carlo et al. 2007). Accordingly, Papautsky's group recently proposed a two-step particle focusing model for the rectangular cross-section channels which is in good agreement with the experimental results (Zhou and Papautsky 2013). However, this model fails to explain the inertial focusing for non-rectangular microchannels such as triangular (Kim et al. 2016). The number of equilibrium positions inside a rectangular channel relies on R_e number ($R_e = \rho_f U_{\max} D_H / \mu$, where ρ_f is the density of fluid, $U_{\max} \approx 2U_{\text{avg}}$ is the maximum flow velocity, and μ is the dynamic viscosity of fluid), aspect ratio ($AR = W/H$, where H and W are height and width of the channel, respectively), and particle clogging ratio, $K = a/H_{\min}$ (Liu et al. 2015). The number of focusing points varies between 2 and 4 at the centers of long and short walls (Bhagat et al. 2008b, c; Chung et al. 2012; Di Carlo et al. 2009; Edd et al. 2008; Hur et al. 2010; Mach and Di Carlo 2010). Mainly two equilibrium positions inside a rectangular microchannel, adjacent to the longer walls, have been utilized for particle filtration (Bhagat et al. 2008b; Zhou et al. 2014), fractionation (Zhou et al. 2013), and flow cytometry (Bhagat et al. 2010a; Oakey et al. 2010) when the AR varies considerably from unity. Recently, experimental results demonstrated that the higher the clogging ratio K ($0.3 \leq K < 0.4$), the higher the AR ($2 \leq AR < 5$) will be to obtain two strong focusing streaks, i.e., narrower particle band width in the middle of long faces of channel (Liu et al. 2015; Reece and Oakey 2016). Generally, as the ratio of AR/K goes up, the particle band width increases (Liu et al. 2015) within the perspective of inertial microfluidics $10 \leq Re \leq 100$ (Amini et al. 2014; Bhagat et al. 2008c; Di Carlo 2009). In this study, AR of 2 and 4 is, therefore, chosen at which the best particle focusing is achieved.

Despite comprehensive experiments and numerical analysis of the lift forces in a rectangular (Di Carlo et al. 2009; Liu et al. 2015) and non-rectangular microchannels (Kim et al. 2016), which all possess planes of symmetry, less effort is made on the “flow field structure” of trapezoidal straight microchannels and its effects on inertial focusing. On the other hand, a rectilinear channel with trapezoidal cross sections breaks down all planes of symmetry. Though trapezoidal cross section has been exclusively applied in curved microchannels to alter the secondary flow structure—thereby improving the separation resolution (Guan et al. 2013; Warkiani et al. 2014a, b; Wu et al. 2012) and filtration (Rafeie et al. 2016)—the channel AR ($AR = W/H_{\min}$) ranged from ~ 7.1 to ~ 12.5 in previous works, which was relatively high, and the slope of slanted wall was limited to low degree ($\tan(\alpha) < 0.1$). Given the simplicity (operation and manufacturing) of straight microchannels compared to

the spiral channels and ease of parallelization, we believe that for certain type of applications, straight microchannels would be better candidates for particle sorting. In this work, inertial focusing was experimentally investigated in a straight microchannel with a trapezoidal cross section—without the presence of curvature-induced secondary flow. The impacts of slanted wall and particle clogging ratio as the two determining factors were mainly studied then. A particle size-dependent lateral focusing shifting toward the longer side wall was found ($Re < 100$). Its major lateral focusing, nonetheless, moved backward to the shorter side wall for high-Re flows. Remarkably, an almost complete transition of particle focusing with $K \sim 0.9$ ($45 \mu\text{m}$) from the longer side wall to the shorter side wall was demonstrated at extremely high particle Re number of $R_p \sim 85$. This phenomenon might shed further light into the mechanism of cross-lateral inertial migration of particles close to the wall (wall-effect lift force) through establishing a comprehensive numerical model in near future. Eventually, as a proof of principle, a trapezoidal straight microchannel was utilized for continuous filtration of a broader range of particle clogging ratio ($0.3 < K < 1$) in comparison with the rectangular straight microchannels ($W > H$, $0.3 \leq K < 0.5$ (Zhou et al. 2014)).

2 Theoretical background

The lateral migration of neutrally buoyant particles dispersed in a fluid flowing through a channel originates from inertial lift force which is decomposed to shear-gradient (F_S) and wall-induced (F_W) lift forces. The inertial effects begin to be dominant if the particle size is comparable to the characteristic channel length, $a/D_H > 0.07$ (Di Carlo et al. 2007). Shear-gradient lift force arises from curvature of velocity profile inside the channel although formation of parabolic velocity profile cannot occur without the presence of the wall (Amini et al. 2014; Zhang et al. 2016). The difference in velocity around the finite-sized particle (Martel and Toner 2014; Zhang et al. 2016) induces a dominating shear-gradient lift force across the channel height ($W > H$). Particles, therefore, migrate toward the top and the bottom wall in the rectangular channels (Fig. 1a). In contrast, due to the dissymmetry in the corresponding trapezoidal channels, the equilibrium plane near the slanted wall is spoiled and thus particles are mainly driven toward the center and the bottom wall (Fig. 1b). In this zone, adjacent to the wall, a cross-lateral wall-effect lift (F_{CL}) is dominant, driving particles toward the center of long wall in the rectangular channels (Zhou and Papautsky 2013; Zhou et al. 2013). Nonetheless, altering the rectangular cross section to the trapezoidal causes an asymmetry in the velocity profile while the core of maximum velocity declines toward the longer side wall, resulting in off-center turning point in the

shear field, whereby lateral focusing shifts toward the longer side wall (Fig. 1b).

According to analytical models developed earlier to justify the particle migration across the streamline (Feng et al. 1994; Ho and Leal 1974), shear-gradient forces are independent of particle rotation (Martel and Toner 2014) and it should be noted that the rotation-induced lift force is 3 orders of magnitude smaller than the shear-gradient lift force (Ho and Leal 1974; Rubinow and Keller 1961). The wall-induced lift force is triggered when the particle approaches the wall. A dissymmetry in pressure distribution around the particle adjacent to the wall pushes back the particle toward the center (Martel and Toner 2014). This dissymmetry in pressure originates from a decelerated fluid flow between the particle and side wall which leads to an increase in pressure (Bernoulli's principle).

The net inertial lift force scales with a^4 which was derived using the perturbation method (Asmolov 1999) based on point-particle approximation, i.e., neglecting finite-sized particle (Di Carlo et al. 2009) as follows:

$$F_L = f_L \frac{\rho U_{\max}^2 a^4}{D_H^2} \quad (1)$$

where f_L is a dimensionless lift coefficient which is a function of particle position for a definite channel cross section and Re number (Di Carlo 2009) which can be decreased by increasing Re number (Lee and Balachandar 2010; Zeng et al. 2009). Recently, it was experimentally shown that f_L in a channel with rectangular cross section can be expressed as follows (Zhou and Papautsky 2013), where $W > H$:

$$f_L \propto \frac{H^2}{a^2 \sqrt{Re}} \quad (2)$$

Therefore, the net inertial lift force F_L scales with a^2 ($F_L \propto a^2$).

3 Materials and methods

3.1 Design and fabrication

To study the new configuration of the inertial lift forces and their impacts on particle focusing within a microchannel with a trapezoidal cross section, we designed a series of trapezoidal channels with $AR = 2$ to 4 while the slopes of upper wall varied from ~ 0.2 to ~ 0.65 (Fig. 1c, $\tan(\alpha) = 0.2\text{--}0.65$). Also, a microchannel with rectangular cross section ($\tan(\alpha) = 0$) was fabricated not only to compare the results but also as a benchmark to verify the well-recognized particle focusing phenomenon for the designed rectangular

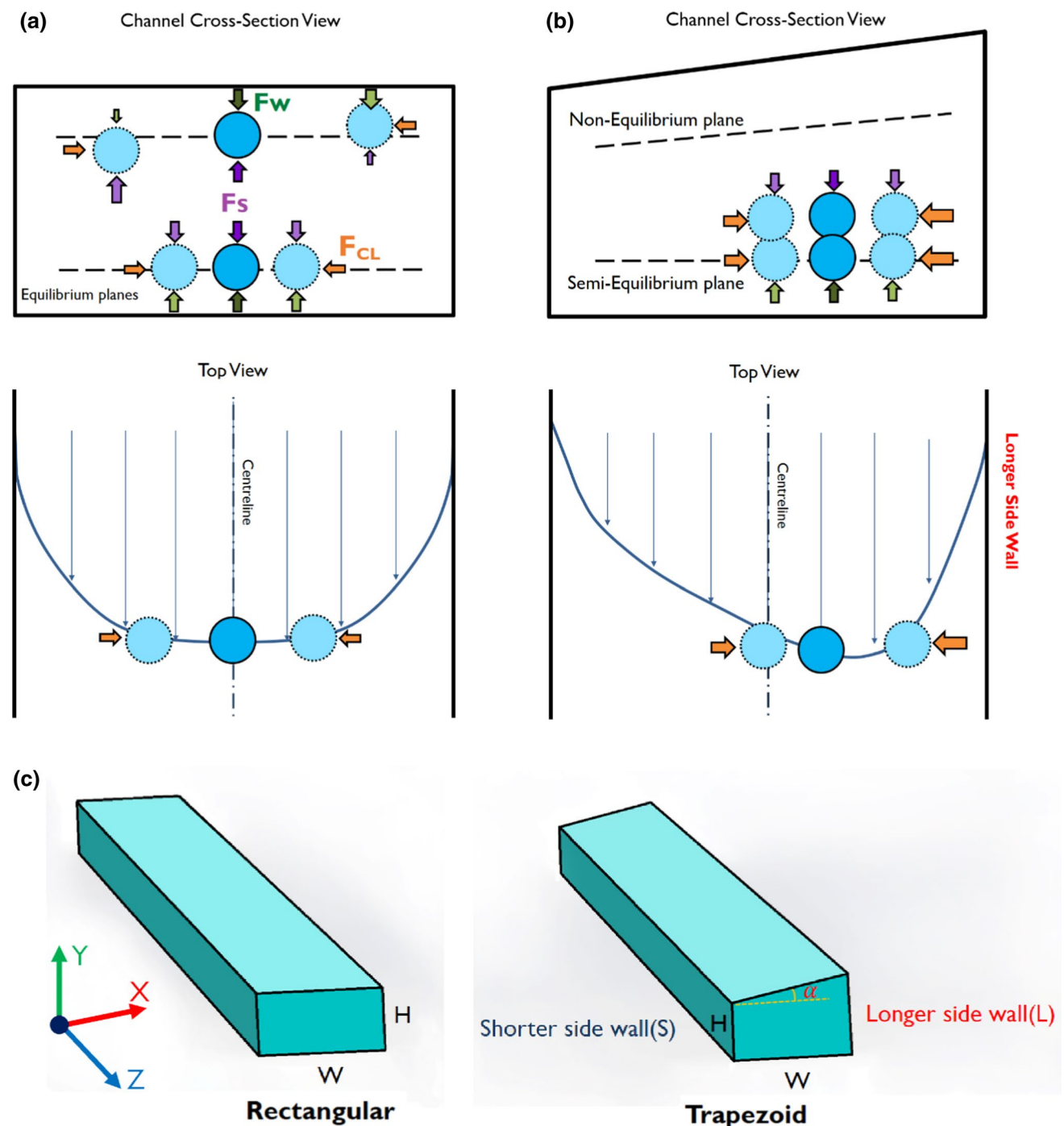


Fig. 1 Schematic representations of shear-gradient lift force (F_S), wall-induced lift force (F_W) and cross-lateral wall-effect lift force (F_{CL}) in **a** a rectangular and **b** a trapezoidal microchannel. **c** Rectangular and trapezoidal straight microchannels designed; slope of the slanted wall is $\tan(\alpha)$

channel. All the microchannels' length is 40 mm, with one inlet and one outlet. The length of microchannels having bifurcation is increased to 60 mm. The height of shorter side wall in the trapezoidal channels which is equal to the rectangular height was chosen to be 50 μm (Fig. 1c). Rectangular microchannels were fabricated using standard soft lithography techniques described elsewhere (Warkiani et al.

2011), while trapezoidal channels were built using micro-milling technique described in our previous works (Warkiani et al. 2014a). The cross sections of all fabricated channels can be seen in Fig. S1. Having been cured in an oven, the polydimethylsiloxane polymer (PDMS, Sylgard 184 Silicone Elastomer Kit, Dow Corning) replica was bonded to another thick layer of PDMS. First, the degassed mixed PDMS and

curing agent (ratio 10:1) were cured for 1.5 h in an oven at 80 °C. Next, after replica and blank layer of PDMS were peeled off, the inlet and outlet were pierced using a Uni-Core™ puncher. Finally, the replica and blank layer were bonded irreversibly by oxygen plasma cleaner (PDC-002, Harrick Plasma) and cured for 3 h in an oven at 70 °C. A 1/50" tubing (Tygon ND-100-80, USA) was used for the inlet and outlet ports.

3.2 Sample preparation

Different neutrally buoyant particle sizes (polystyrene $\rho \sim 1.05$ g/mL), with mean diameters of 10, 20, 45 μm (Fluoresbrite® YG Microspheres, Polysciences Inc, USA), and 15 μm (Dragon green, Bangs Lab Inc, USA), were used to investigate the effect of particle clogging ratio (K) under different flow conditions. Fluorescent particles were diluted with DI water to reach ~ 0.01 – 0.02% volume fraction to decrease the particle–particle interaction. Tween 20 (Sigma-Aldrich, Singapore) was added, at a ratio of $\sim 0.1\%$ volume fraction to avoid particle clogging or particle aggregation.

3.3 Numerical simulations

To investigate the flow field structure within different channel cross-section profiles, a 3D microchannel model was numerically developed using commercial software ANSYS Fluent (Version 15). The Navier–Stokes governing equations were solved for laminar flow using SIMPLE scheme. No-slip boundary condition was applied to wall. The velocity inlet and atmospheric pressure were set to the inlet and outlet, respectively. The physical properties of liquid water, i.e., density of 998.2 kg/m³ and dynamic viscosity of 0.001002 kg/m/s, were used for flow simulation.

3.4 Experimental setup and measurement

Each suspension was pumped through the channel using a syringe pump (Chemyx, F200, USA) at different flow rates from 0.05 to 5 mL/min. The channel was mounted on an inverted epifluorescence microscope (Olympus IX71, Olympus Inc., USA) equipped with 16-bit CMOS camera (optiMOS, QImaging). The images were taken at downstream close to the outlet (~ 40 mm). To capture the trace of fluorescent particles, exposure time was set to 1 s. To statistically find particle streak distribution, on average 100 fluorescent image sequences were stacked using IMAGEJ software to create a composite image along with an intensity line scan across the channel width. Counting particles using hemocytometer could not be carried out accurately for the dilute suspension in an order of 10^4 particles/mL (10, 15 and 20 μm) and 10^3 particles/mL (45 μm). Thus, a smaller sample volume of 1 μL (10–20 μm particle size) and 50 μL

(45 μm particle) was taken for enumerating particles. Having been collected from each outlet, samples were agitated by using vortex mixer and pipetting and then the smaller sample volume was taken and dispersed into a Petri dish. Subsequently, the fluorescent particles were counted manually on the microscope stage using fluorescent illumination.

To eliminate formation of air bubbles inside the channels, all channels required to be first primed by 70% ethanol for ~ 5 min before pumping particle suspension.

4 Results and discussion

4.1 Inertial focusing in the trapezoidal straight channel with AR of 2

To investigate the particle equilibrium position inside a trapezoidal cross section, the effect of trapezoidal cross section on axial velocity and vorticity profile was first studied as the main factors in the first step of particle migration undergoing shear-gradient lift force (Zhou and Papautsky 2013). Figure 2 shows axial velocity contour and two main vorticities whose directions in the plane are perpendicular to the main flow. Shear-gradient inertial lift force originates from curl velocity (Zhou and Papautsky 2013) ($F_S = \omega \times U_S$, where U_S is the particle slip velocity and ω is the curl velocity). ω_x and ω_y are the representative of two major shear rates ($\omega_x \approx \frac{\delta V_{Axial}}{\delta y}$ and $\omega_y \approx -\frac{\delta V_{Axial}}{\delta x}$) which drive particles toward the top/bottom wall and the side walls at the primary stage of lateral migration. The axial velocity contour displays deviation of the maximum velocity inside the trapezoidal cross section toward the longer side wall. This deviation is one of the main factors which results in a new configuration of net inertial force and new equilibrium positions. ω_x contour in Fig. 2a shows no significant change in the symmetrical condition when the rectangular cross section is altered to the trapezoid, the ω_y contour, nonetheless, incurs a noticeable asymmetry along the channel width, particularly when AR increases from 2 to 4 (Fig. 2a, ω_y), leading to the shear-gradient lift forces, pushing particles toward the longer side wall for the trapezoidal cross section (Sect. 4.2), dash lines show zero-shear-rate boundary where direction of shear-gradient lift force alters. Similarly, the corresponding normalized axial velocity profiles show that elevated AR, from 2 to 4, intensifies the asymmetry of the velocity contour for the trapezoidal channels (Fig. 2b). But, increasing the slope of the slanted wall, $\text{Tan}(\alpha)$, from 0.2 to 0.65, cannot change the asymmetry of axial velocity profile considerably; for the AR = 4 (Fig. 2c).

The equilibrium position of 10- μm and 15- μm fluorescent particles ($K \sim 0.2$ – 0.3) is shown for the trapezoidal channel ($H_{SW}50 \mu\text{m}$ - $H_{LW}70 \mu\text{m}$ - $W100 \mu\text{m}$) with AR = 2 in Fig. 3.

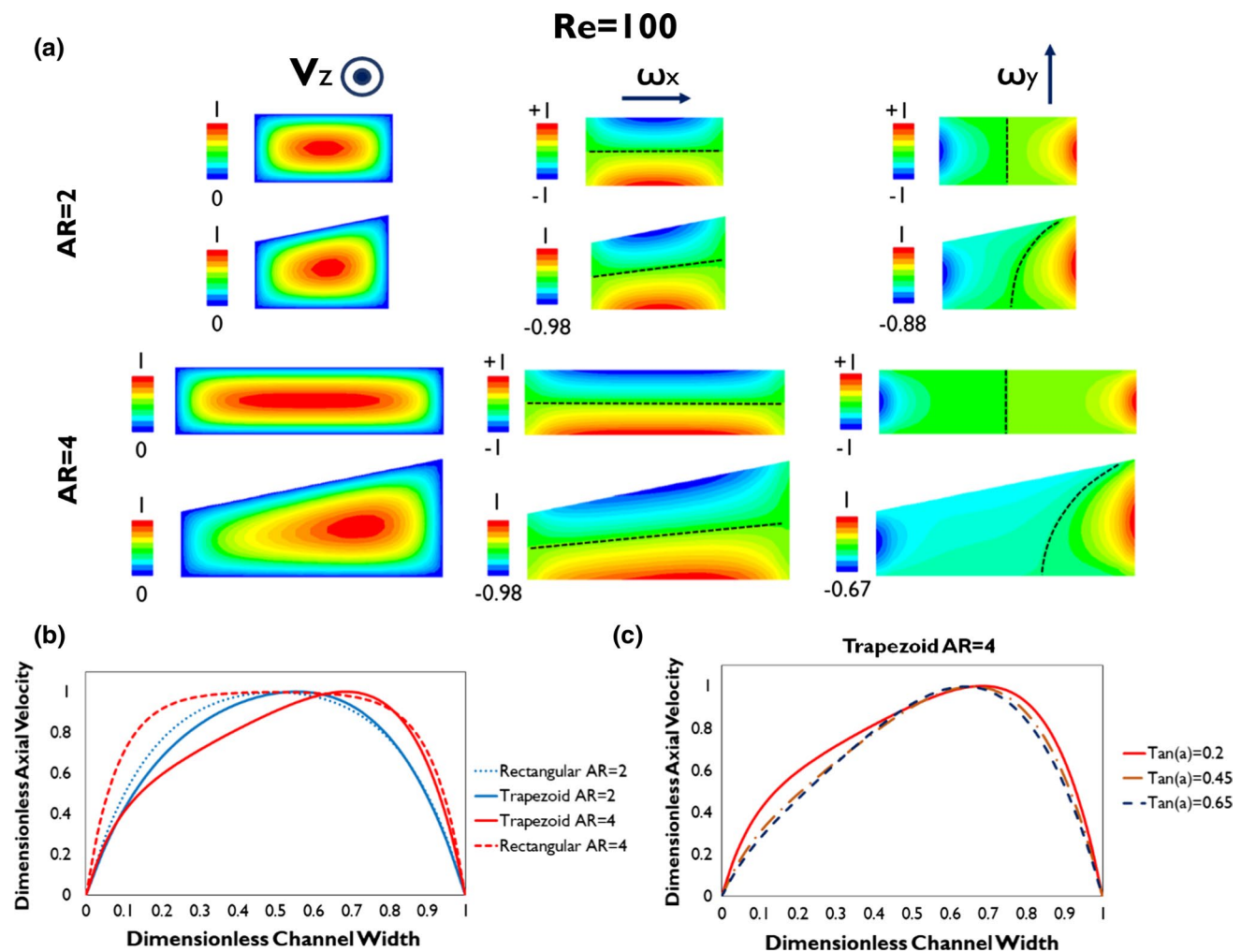


Fig. 2 **a** Normalized axial velocity and vorticity profile at $Re = 100$ for channels with rectangular and trapezoidal cross sections with $\tan(\alpha) = 0.2$. All contours are plotted under the same condition to be comparable qualitatively. Dash lines show zero-shear rate boundary where direction of shear-gradient lift force alternates. **b** The corresponding normalized axial velocity profile for the rectangular and

the trapezoidal channel at the middle of channel height coincided with dash lines at ω_x contour. It shows that the deviation of maximum velocity toward the longer side wall is enhanced by increasing channel AR from 2 to 4. **c** Normalized axial velocity profiles of trapezoidal straight microchannels for increased slopes of the slanted wall at the middle of channel height

As can be seen in Fig. 3a, particles start gradually focusing and migrating toward the longer side wall when Re number increases ($20 \leq Re < 240$). Further increasing Re causes another lateral focusing next to the short side wall ($Re \geq 240$, $K \sim 0.3$), whereas the smaller particles with $K \sim 0.2$ are mostly dispersed due to the lower shear force. These minor lateral particle streams next to the side walls can be seen in Fig. 3b at high $Re = 320$ using intensity line scans. The main lateral focusing peak of $K \sim 0.3$ particles is slightly deviated toward the longer side wall ($80 \leq Re \leq 160$); when exceeding a critical threshold, it causes particles to move back to the middle of the channel. This movement of major lateral focusing point in the trapezoidal channel is illustrated in Fig. 3b by using fluorescence intensity line scan across the channel width. This low off-center movement of the major

lateral focusing ($\sim 10\%$ of the channel width at $Re \sim 80$) in the trapezoidal channel with $AR = 2$ compared to the trapezoidal channel with $AR = 4$, to be investigated next, has qualitatively similar trends to the numerical simulation, showing less dissymmetry in the velocity profile (or shear field).

4.2 Inertial focusing in the trapezoidal straight channel with AR of 4

Particle focusing inside the rectangular channel ($H50 \mu\text{m} \times W200 \mu\text{m}$) with AR of 4 was first investigated as a benchmark ($\tan(\alpha) = 0$). Figure 4a shows the lateral particle stream with $K \sim 0.4$ ($20 \mu\text{m}$) equilibrated at the centers of the long face walls for $Re < 212$. As shown, further

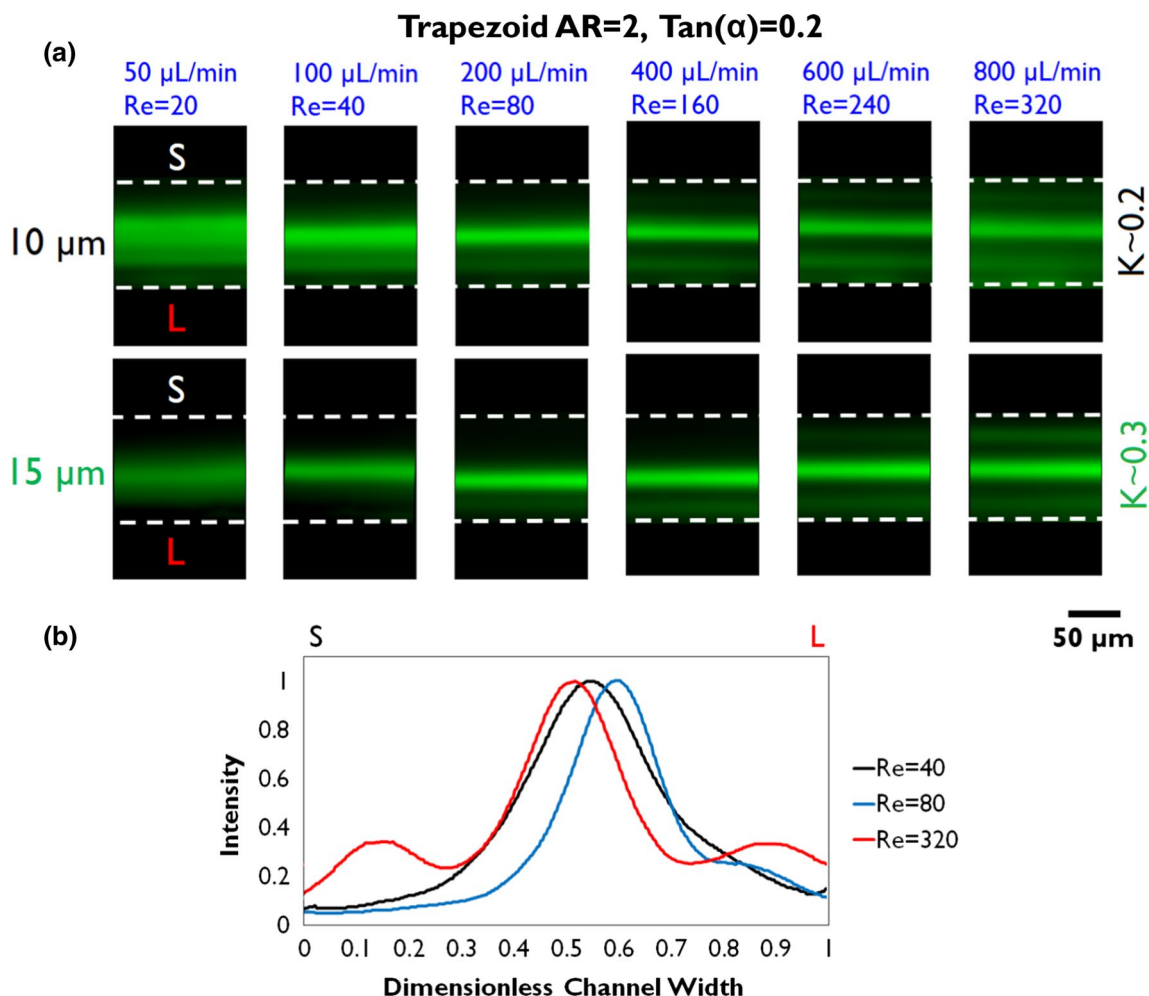


Fig. 3 **a** Fluorescent images of 10- μm ($K \sim 0.2$) and 15- μm ($K \sim 0.3$) microparticles display lateral distribution of particles in the trapezoidal channel with $AR = 2$ and $\text{Tan}(\alpha) = 0.2$, **b** corresponding inten-

sity line scan of 15- μm particles across the channel width (Letter *L* and *S* show the longer and the shorter side wall of the trapezoidal channel, respectively)

increasing Re number causes unstable equilibrium and consequently turns the lateral focusing at the middle into two lateral focusing streams symmetrically ($Re \geq 212$), which can also be seen in the corresponding intensity line scan profile (Fig. 4b). Smaller particle clogging ratio of $K \sim 0.3$ (15 μm) forms a comparatively broader particle band width [See supplementary information Fig. S2(a)] due to less wall-effect lift forces, $F_{CL} \sim a^3$ (Zhou and Papautsky 2013). These behaviors are in agreement with previous works (Liu et al. 2015; Reece and Oakey 2016).

Figure 4c shows that changing the rectangular channel ($\text{Tan}(\alpha) = 0$) to the trapezoidal channel with $\text{Tan}(\alpha) = 0.2$ ($H_{SW} 50 \mu\text{m}$ - $H_{LW} 90 \mu\text{m}$ - $W 200 \mu\text{m}$) slightly enhances the deviation of lateral focusing ($K \sim 0.4$, 20 μm) toward the longer side wall for low $Re \sim 49$, compared with the trapezoidal channel having $AR = 2$ (Fig. 3), but the main lateral focusing gradually gets back to the center of long face wall when Re increases to ~ 196 . Further increasing the channel

Re number leads to the migration of main lateral focusing close to the shorter side wall while some other weaker lateral particle streams simultaneously start to emerge around the middle and the longer side wall ($Re \sim 733$). The movement of major lateral focusing toward the longer side wall and its backward shifting can be seen in Fig. 4d. Also, the minor equilibrium is developed next to the longer side wall as Re exceeds ~ 196 illustrated by small peak adjacent to the wall at Fig. 4d. Particles with lower clogging ratios, less than or equal to $K \sim 0.2$ (10 μm), have no clear lateral focusing and are almost dispersed along the channel width [Fig. S2(b)].

Interestingly, elevating the slope of slanted wall up to $\text{Tan}(\alpha) \sim 0.45$ ($H_{SW} 50 \mu\text{m}$ - $H_{LW} 140 \mu\text{m}$ - $W 200 \mu\text{m}$) further enhances the migration of particles with K greater than or equal to ~ 0.3 toward the longer side wall (Fig. 4e) and boosts their focusing quality (Fig. 4f) for low- Re flows ($Re < 100$). However, minor peaks in Fig. 4f at $Re > 100$ demonstrate that going beyond this threshold of channel Re

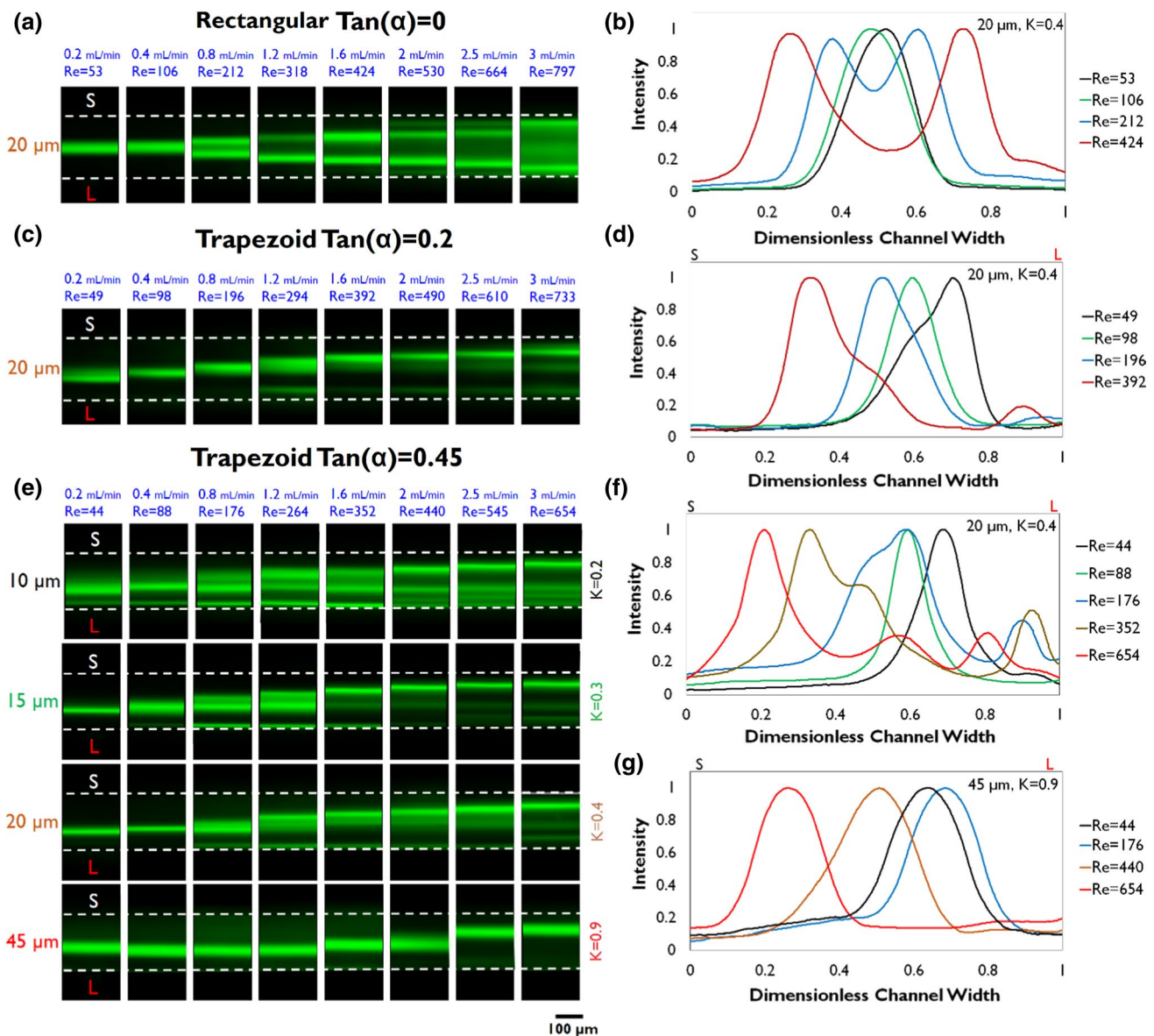


Fig. 4 Fluorescent images and the corresponding intensity line scans of the rectangular channel **a–b** and the trapezoid with $\text{Tan}(\alpha) = 0.2$ **c–d** for 20- μm particles ($K \sim 0.4$). **e** Fluorescent images of various particle sizes in the trapezoidal channel with $\text{Tan}(\alpha) = 0.45$ and the corresponding line scans for **f** 20- μm particles ($K \sim 0.4$) and **g** 45- μm

number intensifies particle dispersion around the channel center and the longer side wall compared to the trapezoidal channel with lower slope ($\text{Tan}(\alpha) \sim 0.2$). Due to the comparatively large slant, it could handle a broader range of particle size without clogging. Figure 4e shows that the lateral focusing of particles with $K \sim 0.9$ (45 μm) sustains higher $\text{Re} \sim 264$ while neighboring the longer side wall. Remarkably, further increasing Re to ~ 654 demonstrates an almost complete shift of the lateral focusing toward the shorter side wall which can also be observed using the intensity line scan (Fig. 4g). It should be noted that the intensity line scan does

not approach zero near the longer wall, representing a few random particles passing by near the longer side wall.

To further clarify the location of particle focusing inside the trapezoidal channels, a side view channel was fabricated. Its fabrication process can be found elsewhere (Kim et al. 2016). Figure 5a shows a side view of two particle streams for large-sized particles of $K \sim 0.9$ ($\text{Re} < 264$), fluctuating near the center and the bottom wall (Smaller particle clogging ratio $K \sim 0.4$ shown at Fig. S3 displays clearly the side view of the lateral streams. For low-slant trapezoid $\text{Tan}(\alpha) \sim 0.2$ particles are mainly equilibrated near

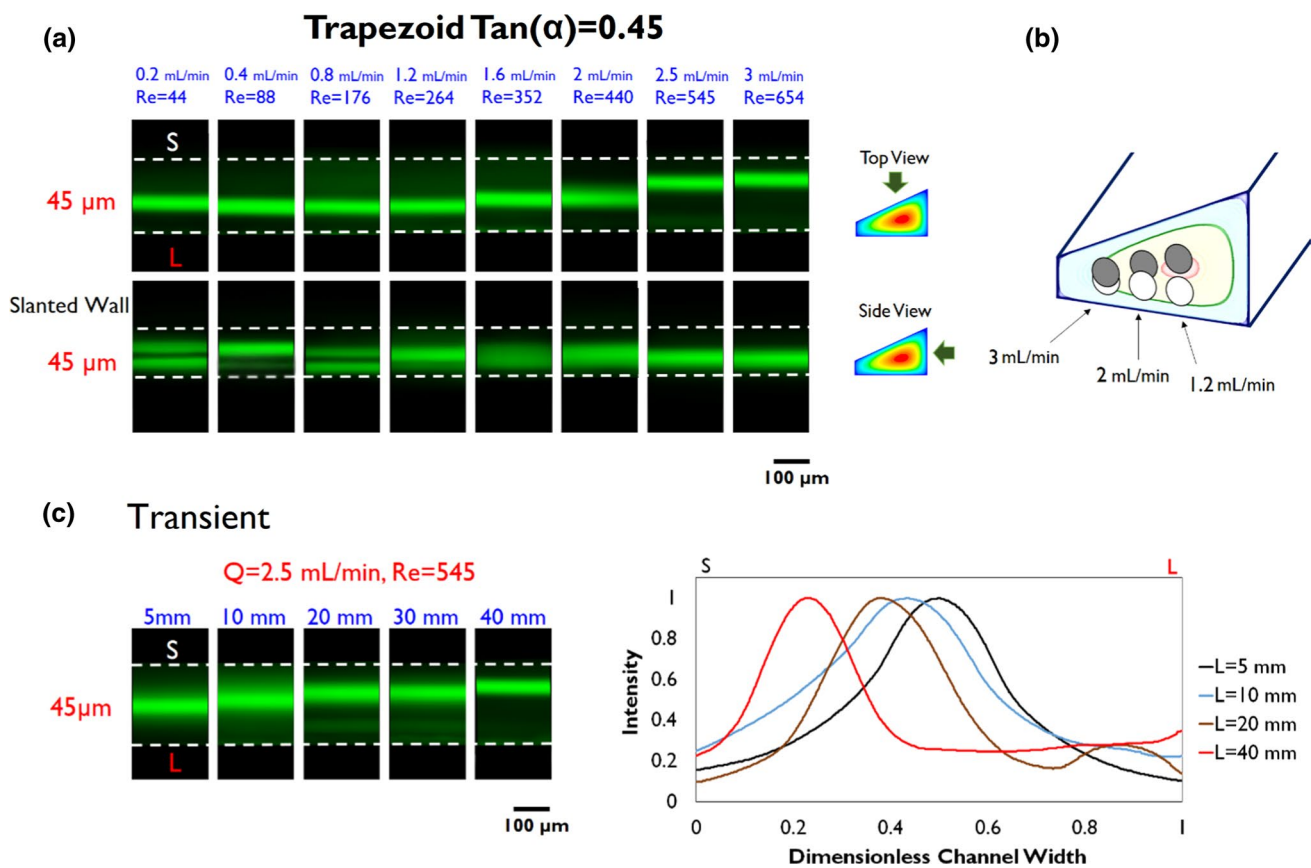


Fig. 5 **a** Top and side views of the particle focusing ($K \sim 0.9$) in the trapezoidal channel with $\text{Tan}(\alpha) = 0.45$ and **b** the corresponding schematic particle movements by increasing Re . **c** Transient lateral particle focusing along the channel length and the corresponding line scans for $\text{Re} \sim 545$ and $K \sim 0.9$. It demonstrates a two-step lateral

movement while it first moves toward the longer side wall and then starts shifting back toward the smaller side wall (Letter L and S show the longer and the shorter side wall of the trapezoidal cross sections, respectively)

the bottom wall and increasing slope of the slanted wall to $\text{Tan}(\alpha) \sim 0.45$ drives particle streams to both the center and the bottom wall.) These two streams gradually merge close to the bottom wall when Re increases to ~ 654 . Figure 5b schematically displays the corresponding shifting of $K \sim 0.9$ particles from the longer side wall to the shorter side wall when Re goes up.

Moreover, the transient lateral particle focusing along the channel length and the corresponding line scan of $K \sim 0.9$ particles are shown in Fig. 5c. Generally, particles are first pushed toward the middle and the longer side wall (see Fig. S4, $\text{Re} \sim 440$ for smaller particle sizes). Afterward, they start to be driven toward the shorter side wall. The developed minor peak next to the longer side wall that is shown in the intensity line scan at $L = 20$ mm gradually disappears, corresponding to particles migrating across streamlines toward the shorter side wall as travel to the channel downstream ($L = 40$ mm). The larger the particle size, the more particles will drift toward the shorter side wall. It should be noted that the particle Re number

is considerably high ($R_p \sim 85$), on the grounds of high $\text{Re} \sim 654$ and large particle size $\sim 45 \mu\text{m}$. We would have interestingly reached the same R_p for the smaller particle size $\sim 20 \mu\text{m}$ if the corresponding channel Re number could go up to ~ 3300 —close to the turbulent flow regime—which is impossible to experimentally explore due to a high pressure drop. Although the unperturbed velocity profile and shear force configuration, when flow is laminar, will remain similar, regardless of its magnitude, the alternation of lateral focusing implies the key role of particle–flow interaction. The particle-induced lateral flow may also play an important role at high- R_p flows (Amini et al. 2012). A comprehensive numerical model which can simulate both particle and flow inertia may lead to an improved understanding of the mechanism of cross-lateral particle movement.

Finally, further increasing the slope of the slanted wall to $\text{Tan}(\alpha) \sim 0.65$ ($H_{\text{SW}} 50 \mu\text{m}$ - $H_{\text{LW}} 180 \mu\text{m}$ - $W 200 \mu\text{m}$) caused a broader range of lateral focusing overall (Fig.

S5) due to the increased hydraulic diameter of channel cross section.

4.3 Particle filtration

Our experimental results proved the size-dependent cross-lateral migration of particles with $K > 0.3$ toward the longer side wall for $Re < 100$. Therefore, a trapezoidal channel with bifurcation was fabricated ($AR \sim 4$ and $\tan(\alpha) \sim 0.45$) for filtration purposes. Figure 6a depicts the filtration of a broad range of particle sizes through the longer wall (LW) outlet. As can be seen, particles with $K \sim 0.3$ ($15 \mu\text{m}$) were approximately equilibrated at the middle, but the majority still went to the LW outlet. The larger particle sizes such as $K \sim 0.4\text{--}0.9$ ($20\text{--}45 \mu\text{m}$) were laterally focused farther away from the middle of channel cross section neighboring the LW and were subsequently collected from the LW outlet. Figure 6b displays the collected samples from the LW and the shorter wall (SW) outlet for $Re \sim 88$ (0.4 mL/min). To quantitatively measure the filtration performance of the trapezoidal straight channel, the efficiency is defined as follows:

$$\text{Efficiency} = \frac{\text{Collected particles of interest}}{\text{Total number of particles}} \quad (3)$$

Total number of particles is the sum of particles collected from both outlets. It should be noted that the ratio of collected volumes from LW to SW outlet is 2:1 due to the skewed maximum velocity toward the LW. The concentration of samples collected from both outlets can be seen in Fig. 6c–e for 15, 20, and 45 μm , respectively. It demonstrates a large gap between concentration of particles collected from LW and SW outlet for particles with $K > 0.3$ ($a > 15 \mu\text{m}$). The corresponding efficiency, Fig. 6f, shows the high efficiency of ~ 99 and $\sim 87\%$ for particles with $K \sim 0.4\text{--}0.9$ and $K \sim 0.3$, respectively, when flow rate is 0.4 mL/min ($Re \sim 88$). The smaller particle size of $10 \mu\text{m}$ ($K \sim 0.2$) cannot be focused, and $\sim 33\%$ of it is diminished through the SW outlet. Thus, filtration resolution of the trapezoidal channel can reach down to $\sim 5 \mu\text{m}$ difference in size, i.e., the trapezoidal channel developed here can focus and filter $\sim 15\text{-}\mu\text{m}$ particle or greater in contrast to smaller particle size of $10 \mu\text{m}$ or less dispersed. Also, the 1.5-fold concentration of the trapezoidal straight channel can potentially increase to twofold by simply cascading two channels, while the whole unit has only one inlet and two outlets, relatively easier than that of the rectangular channels with trifurcation used for filtration (Bhagat et al. 2008b; Mach and Di Carlo 2010; Zhou et al. 2014). In a recent work, a rectangular channel with $AR = 2$ ($W > H$) with higher concentration of threefold to filter $K \sim 0.4$

particles/cells from the center outlet was used (Zhou et al. 2014); nonetheless, the particle clogging ratio could not exceed $K \sim 0.5$ due to the clogging of the channel. Moreover, the rectangular channels with $AR < 1$ ($H > W$) holding similar concentration of 1.5-fold can drive a broad range of particle sizes toward the side walls, $K > 0.07$ (Bhagat et al. 2008c), disregarding being cross-laterally focused. Nonetheless, because of dominating shear-gradient lift force along the channel width, it is likely suitable for extraction of all particle sizes from side outlets while either a particle-free sample or relatively small non-focused particles (such as bacteria in blood (Mach and Di Carlo 2010)) are collected from the central outlet.

Cross-lateral movement of major equilibrium position toward the shorter side wall in the trapezoidal channel can be utilized in filtration applications. A non-symmetrical bifurcation was used to further enhance the concentration of samples collected from the SW outlet, up to \sim threefold, through increasing the volume of carrier fluid extracted from the LW outlet, though being slightly affected. Figure 7a depicts the transition of lateral particle focusing, $K \sim 0.9$ ($45 \mu\text{m}$), from the middle of the channel ($Re \sim 440$) toward the shorter side wall ($Re \sim 1100$), and correspondingly changing the filtration of particles through the LW outlet to the SW outlet at $Re \sim 440$ (2 mL/min) and $Re \sim 1100$ (5 mL/min), respectively (See the Video S1-3†). The transition condition occurred at $Re \sim 880$ (4 mL/min), while the lateral focusing fluctuated around the middle of the channel. Further increasing Re led to migration of particles toward the shorter side wall till Re reached ~ 1100 (5 mL/min); exceeding $Re \sim 1100$ brought about a formation of another lateral focusing near the longer side wall ($Re \sim 1320$). The soaring concentration of collected samples from the SW outlet (~ 2.5 -fold) at $Re \sim 1100$ (5 mL/min) can be seen in Fig. 7b and the corresponding efficiency in Fig. 7c, as high as $\sim 82\%$. It should be noted that the threshold of critical Re number from which particles began to migrate to the shorter side wall was increased for the trapezoidal channel having bifurcation, mainly due to the slight alteration of cross-section dimensions, which arose from the $\pm 10 \mu\text{m}$ resolution of micro-milling technique, and the channel deformation due to the high working pressure. The performance of the device, i.e., efficiency and concentration factor, can be further enhanced by fabricating more precise channels and manipulating the bifurcation design. Also, the filtration resolution can be further enhanced by using a symmetrical trapezoidal cross section, thereby boosting inertial focusing off the channel center even at higher Re number expected.

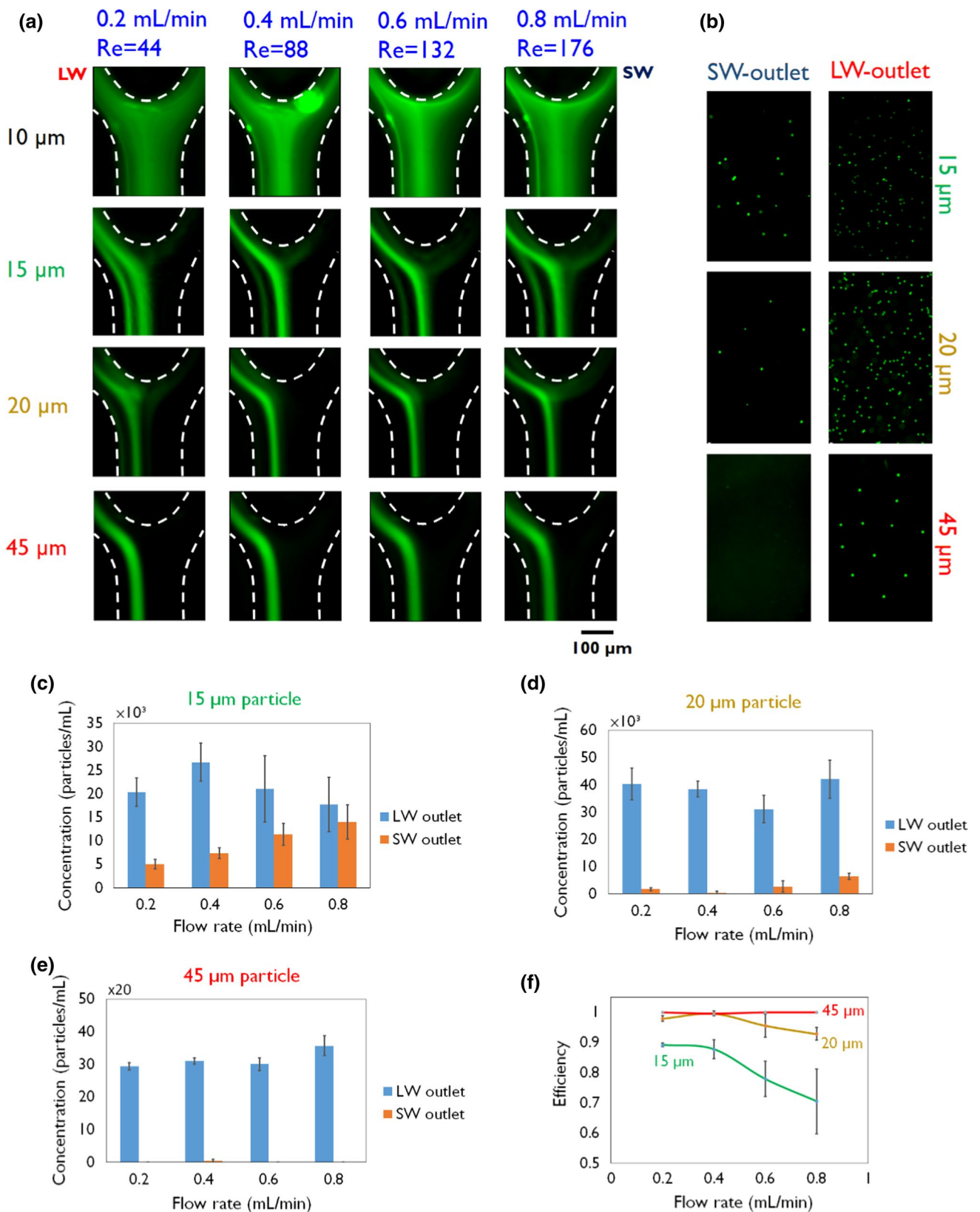


Fig. 6 **a** Lateral focusing and filtration of particles through the longer wall outlet in the trapezoidal straight channel ($\tan(\alpha) \sim 0.45$ and $AR \sim 4$), and **b** the corresponding samples collected from the shorter wall (SW) outlet and the longer wall (LW) outlet at $Re \sim 88$ (0.4 mL/

min). **c–e** Concentration of various particle sizes (15, 20 and 45 μm) collected from the SW outlet and the LW outlet. **f** Efficiency of particle filtration versus flow rate

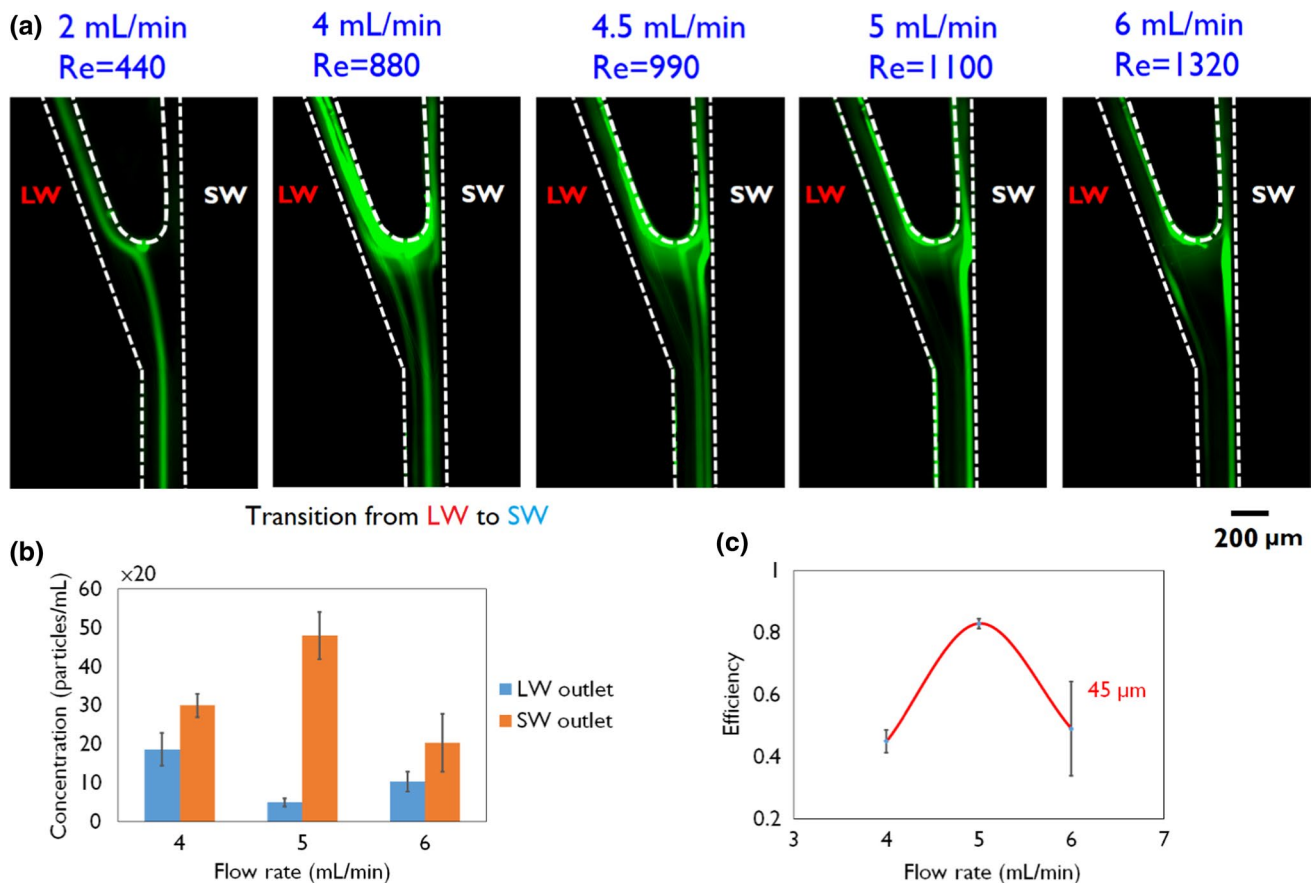


Fig. 7 **a** Transition of lateral focusing from the middle of channel cross section toward the shorter side wall as the Re number increases. **b** Concentration of samples collected from the SW and the LW out-

let and **c** the corresponding efficiency (Letter LW and SW show the longer and the shorter wall outlet of the trapezoidal cross section ($\tan(\alpha) \sim 0.45$ and $AR \sim 4$), respectively)

5 Conclusion

In this work, we investigated the inertial particle focusing dynamics in trapezoidal straight microchannels for a broad range of channel Reynolds number ($20 < Re < 800$) and various slopes of slanted walls. Increasing the aspect ratio (AR) from 2 to 4 enhanced the off-center lateral focusing position from the middle of channel cross section, up to $\sim 20\%$ of the channel width (Fig. 4f). A size-dependent lateral focusing position first shifted toward the longer side wall and then moved back toward the shorter side wall when Re was progressively increased ($Re > 50$). It was found that the focusing point was spoiled near the slanted wall due to the dissymmetry; the focusing was mainly developed near the bottom wall or fluctuated between the channel center and the bottom wall, depending on the slanted wall and Re ($Re < 100$, channel aspect ratio 4:1). Remarkably, an almost complete shift in major focusing from the longer side wall to the shorter side wall was found for the large particle clogging ratio of $K \sim 0.9$ ($K = a/H_{\min}$) when Re increased noticeably to ~ 650 . Eventually, the

trapezoidal straight channel ($AR \sim 4$ and $\tan(\alpha) \sim 0.45$) along with a bifurcation was used for continuous filtration of a broad range of particle size ($0.3 < K < 1$) exiting through the longer wall outlet with an efficiency of $\sim 99\%$ ($Re < 100$). Finally, filtration of large-sized particles with $K \sim 0.9$ through the shorter wall outlet was shown at extremely high $Re \sim 1100$ with $\sim 82\%$ efficiency and ~ 2.5 -fold concentration.

Acknowledgements The first author would like to thank the SINGA scholarship sponsorship by A*STAR graduate academy, Singapore. This work was performed (in part) at the NSW and South Australian node of the Australian National Fabrication Facility under the National Collaborative Research Infrastructure Strategy to provide nano- and micro-fabrication facilities for Australia's researchers. M.E.W. would like to acknowledge the support of the Australian Research Council through Discovery Project Grants (DP170103704 and DP180103003) and the National Health and Medical Research Council through the Career Development Fellowship (APP1143377).

References

- Amini H, Sollier E, Weaver WM, Di Carlo D (2012) Intrinsic particle-induced lateral transport in microchannels. *Proc Natl Acad Sci USA* 109:11593
- Amini H, Lee W, Di Carlo D (2014) Inertial microfluidic physics. *Lab Chip* 14:2739–2761. <https://doi.org/10.1039/C4LC00128A>
- Asmolov E (1999) The inertial lift on a spherical particle in a plane Poiseuille flow at large channel Reynolds number. *J Fluid Mech* 381:63
- Bhagat A, Kuntaegowdanahalli S, Papautsky I (2008a) Continuous particle separation in spiral microchannels using dean flows and differential migration. *Lab Chip* 8:1906
- Bhagat A, Kuntaegowdanahalli S, Papautsky I (2008b) Enhanced particle filtration in straight microchannels using shear-modulated inertial migration. *Phys Fluids* 20:101702
- Bhagat AAS, Kuntaegowdanahalli SS, Papautsky I (2008c) Inertial microfluidics for continuous particle filtration and extraction. *Microfluid Nanofluid* 7:217–226. <https://doi.org/10.1007/s10404-008-0377-2>
- Bhagat A, Kuntaegowdanahalli SS, Kaval N, Seliskar CJ, Papautsky I (2010a) Inertial microfluidics for sheath-less high-throughput flow cytometry. *Biomed Microdevices* 12:187
- Bhagat AAS, Bow H, Hou HW, Tan SJ, Han J, Lim CT (2010b) Microfluidics for cell separation. *Med Biol Eng Comput* 48:999–1014
- Bhagat AAS, Kuntaegowdanahalli SS, Kaval N, Seliskar CJ, Papautsky I (2010c) Inertial microfluidics for sheath-less high-throughput flow cytometry. *Biomed Microdevice* 12:187–195
- Chen H, Wang L, Li PC (2008) Nucleic acid microarrays created in the double-spiral format on a circular microfluidic disk. *Lab Chip* 8:826–829
- Chung A, Gossett DR, Di Carlo D (2012) Three dimensional, sheath-less, and high-throughput microparticle inertial focusing through geometry-induced secondary flows. *Small* 9:685
- Destgeer G, Lee KH, Jung JH, Alazzam A, Sung HJ (2013) Continuous separation of particles in a PDMS microfluidic channel via traveling surface acoustic waves (TSAW). *Lab Chip* 13:4210–4216. <https://doi.org/10.1039/C3LC50451D>
- Di Carlo D (2009) Inertial microfluidics. *Lab Chip* 9:3038
- Di Carlo D, Irimia D, Tompkins R, Toner M (2007) Continuous inertial focusing, ordering, and separation of particles in microchannels. *Proc Natl Acad Sci USA* 104:18892
- Di Carlo D, Edd J, Humphry K, Stone H, Toner M (2009) Particle segregation and dynamics in confined flows. *Phys Rev Lett* 102:094503
- Edd JF, Di Carlo D, Humphry KJ, Koster S, Irimia D, Weitz DA, Toner M (2008) Controlled encapsulation of single-cells into monodisperse picolitre drops. *Lab Chip* 8:1262–1264. <https://doi.org/10.1039/b805456h>
- Feng J, Hu HH, Joseph DD (1994) Direct simulation of initial value problems for the motion of solid bodies in a Newtonian fluid Part 1. Sedimentation. *J Fluid Mech* 261:95–134
- Guan G, Wu L, Bhagat AA, Li Z, Chen PCY (2013) Spiral microchannel with rectangular and trapezoidal cross-sections for size based particle separation. *Sci Rep* 3:1495
- Ho B, Leal L (1974) Inertial migration of rigid spheres in two-dimensional unidirectional flows. *J Fluid Mech* 65:365
- Hur SC, Tse HT, Di Carlo D (2010) Sheathless inertial cell ordering for extreme throughput flow cytometry. *Lab Chip* 10:274–280. <https://doi.org/10.1039/b919495a>
- Hur SC, Mach AJ, Di Carlo D (2011) High-throughput size-based rare cell enrichment using microscale vortices. *Biomicrofluidics* 5:022206
- Kim J, Lee J, Wu C, Nam S, Di Carlo D, Lee W (2016) Inertial focusing in non-rectangular cross-section microchannels and manipulation of accessible focusing positions. *Lab Chip* 16:992–1001. <https://doi.org/10.1039/C5LC01100K>
- Kralj J, Lis M, Schmidt M, Jensen K (2006) Continuous dielectrophoretic size-based particle sorting. *Anal Chem* 78:5019
- Lee H, Balachandar S (2010) Drag and lift forces on a spherical particle moving on a wall in a shear flow at finite Re. *J Fluid Mech* 657:89–125. <https://doi.org/10.1017/S0022112010001382>
- Lee MG, Choi S, Park JK (2011) Inertial separation in a contraction-expansion array microchannel. *J Chromatogr A* 1218:4138–4143. <https://doi.org/10.1016/j.chroma.2010.11.081>
- Liu C, Hu G, Jiang X, Sun J (2015) Inertial focusing of spherical particles in rectangular microchannels over a wide range of Reynolds numbers. *Lab Chip* 15:1168–1177. <https://doi.org/10.1039/C4LC01216J>
- Ma Z, Collins DJ, Ai Y (2016) Detachable acoustofluidic system for particle separation via a traveling surface acoustic wave. *Anal Chem* 88:5316–5323. <https://doi.org/10.1021/acs.analchem.6b00605>
- Mach A, Di Carlo D (2010) Continuous scalable blood filtration device using inertial microfluidics. *Biotechnol Bioeng* 107:302
- Martel JM, Toner M (2013) Particle focusing in curved microfluidic channels. *Sci Rep* 3:3340
- Martel JM, Toner M (2014) Inertial focusing in microfluidics. *Annu Rev Biomed Eng* 16:371–396. <https://doi.org/10.1146/annurev-bioeng-121813-120704>
- Murthy SN (1999) Magnetophoresis: an approach to enhance transdermal drug diffusion. *Pharmazie* 54:377–379
- Nilsson A, Petersson F, Jonsson H, Laurell T (2004) Acoustic control of suspended particles in micro fluidic chips. *Lab Chip* 4:131–135. <https://doi.org/10.1039/B313493H>
- Oakey J, Applegate R, Arellano E, Di Carlo D (2010) Particle focusing in staged inertial microfluidic devices for flow cytometry. *Anal Chem* 82:3862
- Pamme N, Manz A (2004) On-chip free-flow magnetophoresis: continuous flow separation of magnetic particles and agglomerates. *Anal Chem* 76:7250–7256
- Park JS, Song SH, Jung HI (2009) Continuous focusing of microparticles using inertial lift force and vorticity via multi-orifice microfluidic channels. *Lab Chip* 9:939–948. <https://doi.org/10.1039/b813952k>
- Petersson F, Åberg L, Swärd-Nilsson AM, Laurell T (2007) Free flow acoustophoresis: microfluidic-based mode of particle and cell separation. *Anal Chem* 79:5117
- Rafeie M, Zhang J, Asadnia M, Li W, Warkiani ME (2016) Multiplexing slanted spiral microchannels for ultra-fast blood plasma separation. *Lab Chip* 16:2791–2802. <https://doi.org/10.1039/c6lc00713a>
- Reece AE, Oakey J (2016) Long-range forces affecting equilibrium inertial focusing behavior in straight high aspect ratio microfluidic channels. *Phys Fluids* 28:043303. <https://doi.org/10.1063/1.4946829>
- Rubinow S, Keller J (1961) The transverse force on a spinning sphere moving in a viscous fluid. *J Fluid Mech* 11:447
- Sajeesh P, Sen AK (2014) Particle separation and sorting in microfluidic devices: a review. *Microfluid Nanofluid* 17:1–52
- Schonberg JA, Hinch EJ (1989) Inertial migration of a sphere in Poiseuille flow. *J Fluid Mech* 203:517–524. <https://doi.org/10.1017/S0022112089001564>
- Segré G, Silberberg A (1961) Radial particle displacements in Poiseuille flow of suspensions. *Nature* 189:209
- Segré G, Silberberg A (1962) Behaviour of macroscopic rigid spheres in Poiseuille flow Part 2. Experimental results and interpretation.

- J Fluid Mech 14:136–157. <https://doi.org/10.1017/S0022112062001111>
- Sim TS, Kwon K, Park JC, Lee JG, Jung HI (2011) Multistage-multiorifice flow fractionation (MS-MOFF): continuous size-based separation of microspheres using multiple series of contraction/expansion microchannels. *Lab Chip* 11:93–99. <https://doi.org/10.1039/c0lc00109k>
- Situma C, Hashimoto M, Soper SA (2006) Merging microfluidics with microarray-based bioassays. *Biomol Eng* 23:213–231
- Sudarsan AP, Ugaz VM (2006) Fluid mixing in planar spiral microchannels. *Lab Chip* 6:74–82
- Vasseur P, Cox R (1976) The lateral migration of a spherical particle in two-dimensional shear flows. *J Fluid Mech* 78:385
- Voldman J (2006) Electrical forces for microscale cell manipulation. *Annu Rev Biomed Eng* 8:425
- Wang L, Li PC (2011) Microfluidic DNA microarray analysis: a review. *Anal Chim Acta* 687:12–27
- Warkiani ME, Lou C-P, Gong H-Q (2011) Fabrication and characterization of a microporous polymeric micro-filter for isolation of *Cryptosporidium parvum* oocysts. *J Micromech Microeng* 21:035002
- Warkiani ME, Lou C-P, Liu H-B, Gong H-Q (2012) A high-flux isopore micro-fabricated membrane for effective concentration and recovering of waterborne pathogens. *Biomed Microdevice* 14:669–677
- Warkiani ME et al (2014a) Slanted spiral microfluidics for the ultrafast, label-free isolation of circulating tumor cells. *Lab Chip* 14:128–137. <https://doi.org/10.1039/C3LC50617G>
- Warkiani ME et al (2014b) An ultra-high-throughput spiral microfluidic biochip for the enrichment of circulating tumor cells. *Analyst* 139:3245–3255. <https://doi.org/10.1039/C4AN00355A>
- Warkiani ME, Wu L, Tay AKP, Han J (2015) Large volume microfluidic cell sorting. *Annu Rev Biomed Eng*. <https://doi.org/10.1146/annurev-bioeng-071114-040818>
- Wu L, Guan G, Hou H, Bhagat A, Han J (2012) Separation of leukocytes from blood using spiral channel with trapezoid cross-section. *Anal Chem* 84:9324
- Wu Z, Chen Y, Wang M, Chung AJ (2016) Continuous inertial micro-particle and blood cell separation in straight channels with local microstructures. *Lab Chip* 16:532–542. <https://doi.org/10.1039/c5lc01435b>
- Yang Y, Liu AQ, Lei L, Chin LK, Ohl CD, Wang QJ, Yoon HS (2011) A tunable 3D optofluidic waveguide dye laser via two centrifugal Dean flow streams. *Lab Chip* 11:3182–3187. <https://doi.org/10.1039/c1lc20435a>
- Zeng L, Najjar F, Balachandar S, Fischer P (2009) Forces on a finite-sized particle located close to a wall in a linear shear flow. *Phys Fluids* 21:033302
- Zhang J, Li W, Li M, Alici G, Nguyen N-T (2014a) Particle inertial focusing and its mechanism in a serpentine microchannel. *Microfluid Nanofluid* 17:305–316. <https://doi.org/10.1007/s10404-013-1306-6>
- Zhang J, Yan S, Sluyter R, Li W, Alici G, Nguyen N-T (2014b) Inertial particle separation by differential equilibrium positions in a symmetrical serpentine micro-channel. *Sci Rep* 4:4527. <https://doi.org/10.1038/srep04527>
- Zhang J, Yan S, Yuan D, Alici G, Nguyen NT, Ebrahimi Warkiani M, Li W (2016) Fundamentals and applications of inertial microfluidics: a review. *Lab Chip* 16:10–34. <https://doi.org/10.1039/c5lc01159k>
- Zhou J, Papautsky I (2013) Fundamentals of inertial focusing in microchannels. *Lab Chip* 13:1121
- Zhou J, Giridhar PV, Kasper S, Papautsky I (2013) Modulation of aspect ratio for complete separation in an inertial microfluidic channel. *Lab Chip* 13:1919
- Zhou J, Giridhar PV, Kasper S, Papautsky I (2014) Modulation of rotation-induced lift force for cell filtration in a low aspect ratio microchannel. *Biomicrofluidics* 8:044112. <https://doi.org/10.1063/1.4891599>
- Zhu J, Tzeng T-RJ, Xuan X (2010) Continuous dielectrophoretic separation of particles in a spiral microchannel. *Electrophoresis* 31:1382